J. Biophotonics **6**, No. 6–7, 493–504 (2013) / **DOI** 10.1002/jbio.201200204

Journal of BIOPHOTONICS

FULL ARTICLE

Intra-operative *ex vivo* photoacoustic nodal staging in a rat model using a clinical superparamagnetic iron oxide nanoparticle dispersion

Diederik J. Grootendorst[*,1], *Raluca M. Fratila*[2], *Martijn Visscher*[2], *Bennie Ten Haken*[2], *Richard J. A. van Wezel*[3], *Sven Rottenberg*[4], *Wiendelt Steenbergen*[1], *Srirang Manohar*[1], *and Theo J. M. Ruers*[4,5]

[1] Biomedical Photonic Imaging Group, MIRA Institute for Biomedical Technology and Technical Medicine, Faculty of Science and Technology, University of Twente, P.O. Box 217, 7500 AE Enschede, The Netherlands
[2] Neuro IMaging group, MIRA Institute for Biomedical Technology and Technical Medicine, Faculty of Science and Technology, University of Twente, P.O. Box 217, 7500 AE Enschede, The Netherlands
[3] Biomedical Signals and Systems group, Faculty of Electrical Engineering, Mathematics and Computer Science, P.O. Box 217, 7500 AE Enschede, The Netherlands and Donders Institute for Brain, Cognition and Behaviour, Radboud University Nijmegen, P.O. Box 9104, 6500 HE Nijmegen
[4] Netherlands Cancer Institute – Antoni van Leeuwenhoek Hospital (NKI-AVL), The Netherlands
[5] Nanobiophysics Group, MIRA Institute for Biomedical Technology and Technical Medicine, Faculty of Science and Technology, University of Twente, P.O. Box 217, 7500 AE Enschede, The Netherlands

Received 20 October 2012, revised 28 November 2012, accepted 17 December 2012
Published online 24 January 2013

Key words: Photoacoustic, lymph node, staging, intra-operative, SPIO, optoacoustic, oncology

The ability to accurately detect tumor metastases in lymph nodes is essential for intra-operative staging of various malignancies. Histopathological assessment of nodes has the drawback of a time delay before results are available to the surgeon and a likelihood of missing metastases. Photoacoustic (PA) imaging has been shown to possess the potential to detect melanoma metastases in resected *in toto* lymph nodes based on intrinsic contrast. To extend application of the method to other malignancies, extrinsic contrast for lymphatic mapping is important. We investigate in a metastatic animal model whether clinically approved superparamagnetic iron oxide (SPIO) nanoparticles, applied for MRI, can help PA imaging for staging in an intra-operative ex vivo setting. Imaging results are compared with 14 Tesla MR images and histology. We observe that irregularities in SPIO distribution in PA images of the nodes and a decrease in contrast correlate with metastatic involvement as seen in MR images and histology. The results show that a PA based imaging technique may be valuable for nodal staging in the field of surgical oncology.

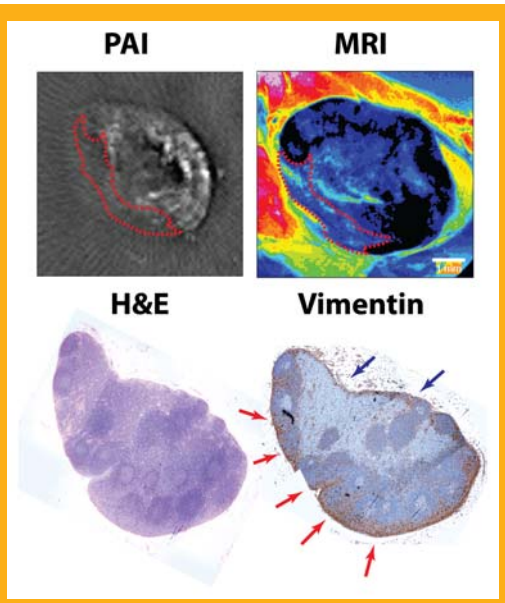

PA and MR images compared with both H & E and Vimentin histology staining for node 1.

* Corresponding author: e-mail: d.j.grootendorst@utwente.nl

Journal of
BIOPHOTONICS

1. Introduction

The presence of lymphatic metastases is a predictor of poor outcome in many solid malignancies [1–4]. Metastasis positive lymph nodes are associated with a decrease of the 5-year survival of melanoma patients, independent of other prognostic factors of the primary tumor [5]. Likewise, the number of resected metastatic lymph nodes correlates with survival in breast cancer patients [6]. Despite the importance of lymph node metastases as highlighted by its inclusion in cancer staging systems, both detection and treatment remain far from optimal.

Superparamagnetic iron oxide nanoparticle (SPIO) enhanced MRI has been proven to detect small and otherwise undetectable lymph node metastases in patients with prostate cancer [7], providing a possibility to improve early diagnosis and decision making. In addition, this approach has also been proven to be of additional benefit for head and neck, breast and pelvis lymph node assessment showing an overall sensitivity of 88% and an overall specificity of 96% based on 19 prospective studies [8]. After subcutaneous or intravenous injection, SPIOs are cleared by draining lymphatic vessels and transported to the lymph nodes where they are phagocytosed by nodal macrophages. Inhomogeneities in SPIO distribution in a lymph node arise once metastatic cells displace the normal nodal architecture. MRI is able to visualize this displacement due to the longer relaxation times arising from the absence of SPIOs at these locations and can be used to distinguish benign from metastatic lymph nodes. The dissimilarity in SPIO distribution between benign and metastatic nodes is schematically displayed in Figure 1.

The success of the approach in pre-operative staging together with the fact that coated SPIOs contain a satisfactory safety profile for human applications [9] have cleared several SPIO dispersions for clinical use. However, MRI is unable to detect micrometastases of less than 1 mm in size using a conventional 1.5 Tesla system [10] in pre- or intra-operative staging. The latter is important for decision making towards the nature of therapy and surgery to be performed. The availability of diagnostic information during the surgical procedure could for example, limit the number of resected lymph nodes during lymphadenectomies or offer the potential to perform a lymphadenectomy directly after sentinel lymph node resection. Both can reduce morbidity while saving time and funds.

Photoacoustic (PA) imaging, an emerging powerful imaging modality that uses optical absorption contrast and posseses ultrasonic resolution, is being widely applied within biomedical research [11, 12]. PA imaging relies on the detection of acoustic waves produced by the thermoelastic expansion of tissue following absorption of short pulsed optical illumination. By this mechanism, PA uncouples signal generation and detection since diffuse light excites ultrasound which can be detected with high resolution. Therefore, PA is able to obtain high resolution images using diffused light from deeper within biological samples compared to purely optical based techniques. In addition, in biological tissue, ultrasonic scattering is about two to three orders of magnitude weaker than optical scattering, resulting in a high spatial resolution. The fact that PA imaging makes no use of ionizing radiation and enables fast imaging performance, could facilitate its introduction as an additional medical imaging technique.

PA imaging can both be based on endogenous biomolecules with natural PA contrast properties (e.g. hemoglobin, melanin), or exogenous contrast

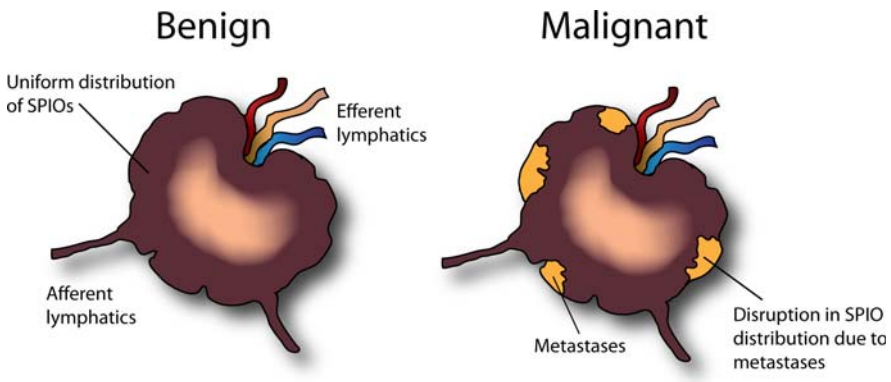

Figure 1 Schematic of the nodal metastases detection scheme using SPIO nanoparticles. In a benign case, the SPIO particles accumulated in a regular pattern in the cortical zone of the lymph node through macrophage uptake 24 hours after injection. Accumulation is mostly centered in the cortical zone of the node due to the particle size of the SPIO agent. In a metastatic case, homogenous distribution of the particles is disrupted in locations where metastatic cells have replaced normal nodal architecture. These irregularities can be visualized with MRI due to differences in relaxation times between nodal tissue with and without SPIOs.

agents delivered by injection. The strong PA response of many endogenous biomolecules enables the visualization of the vasculature associated with breast carcinoma [13–16] or, for example the detection of melanoma cells [17] and melanoma metastases [18, 19]. Exogenous agents, on the other hand, are mostly applied to improve contrast, where the tissue lacks endogenous chromophores related to the studied disease state, including many malignancies [20–22]. To this end, several contrast agents, including nano-materials [23–25], are the subject of extensive research to analyze their benefit in the imaging of specific disease states. Research into the PA imaging of the lymphatics using contrast agents is mostly centered around the mapping of the sentinel lymph node(s) (SLN(s)) [26–29]. Recently, Akers et al. visualized the SLN of rats after methylene blue injection and verified their results using SPECT/CT [30]. Pan et al. proved that copper nanoparticles can be used to enhance and visualize SLN(s) *in vivo* using PA imaging [31].

While showing promising results, most PA contrast agents are as yet in an experimental stage and would require extensive approval procedures before being approved for clinical use by the Food and Drugs Administration (FDA) or European Medicines Agency (EMA). SPIOs on the other hand have been cleared for clinical use and their lymphatic metastasis detection potential has been verified by several clinical MRI studies [7, 8] making them potentially valuable for intra-operative lymph node staging. Based on this, intra-operative staging of lymph nodes as researched by several other optical techniques like Optical Coherence Tomography (OCT) [32] and Raman spectroscopy [33], could possibly also be performed using the combination of photoacoustic imaging and SPIO nanoparticles. This would mean that freshly resected nodes could be scanned during the operation, offering direct diagnostic information to the surgical team. The increased penetration potential of PA imaging compared to optical techniques ensures imaging of the entire nodal volume without requiring the nodes to be sliced or damaged, retaining the possibility to perform (immuno)histochemical analysis postoperatively.

In order to explore this concept, our group recently used clinical SPIO dispersions in healthy rodents to verify that these deposits could be detected with PA. It was shown that the distribution of SPIOs could be mapped with accuracy down to an amount of approximately 11 µg, corresponding with a concentration of 0.8 mg/ml [34]. With regard to the clinical potential of intra-operative lymph node staging using a combination of PA imaging and SPIOs, it however remains to be investigated whether, and on what basis, such a combination is able to make a distinction between benign and metastatic nodes.

In this work, we investigate whether lymph nodes metastases can be visualized with PA imaging after the subcutaneous injection of a clinically approved SPIO dispersion (Endorem®) in a metastatic animal model. Distinctive differences between benign and metastatic nodes are identified and PA imaging results are compared with high field MR images. Findings are verified by way of (immuno)histochemistry and limitations are discussed. In addition, we quantify the SPIO amounts inside the nodes using PA and correlate them to quantitative iron measurements. These experiments could produce the information needed to validate whether PA staging of lymph nodes can be performed with iron oxide nanoparticles. Overall, this could pave the way for the introduction of a PA based imaging technique in the field of surgical oncology.

2. Materials and methods

2.1 Animal model and tumor cell line

All experiments were approved by the local Animal Care Committee. Female Copenhagen rats, weighing 150–200 g were subcutaneously injected with R3327 MAT-LyLu cells in their left hindpaw. The R3327 MAT LyLu prostate tumor variant has been used as an experimental model for syngeneic progression and metastasis of prostate adenocarcinoma. This model has also been frequently used to validate the potential of SPIO agents in MRI [35, 36]. *In vivo*, this tumor is characterized by a rapid and hormone-independent proliferation, anaplastic histology, and metastases to draining lymph nodes and lungs.

For the experiments, cells were cultured in RPMI-1640 medium, supplemented with 10% fetal calf serum and 100 ml penicillin/streptomycin. One million R3327 MAT LyLu tumor cells were dispersed in 0.1 mL of medium and inoculated aseptically in eight Copenhagen rats. The animals were separated into two groups depending on when a subcutaneous injection of 0.1 ml of SPIOs (11.2 g/l) (Endorem®, Guerbet, France) was administered in both hindpaws. The Endorem® particles are composed of several randomly clustered iron oxide cores (diameter 4–6 nm) embedded in a dextran coating [37]. Particles have an estimated hydrodynamic size of 80–150 nm [38]. The extinction spectrum of an Endorem® dispersion is displayed in Figure 2. In the first animal group SPIOs were administered 5 days after tumor inoculation (minor metastatic group), while the second group received injections 8 days after inoculation (major metastatic group). Time spans were chosen according to a pilot study which showed that the popliteal lymph nodes were totally

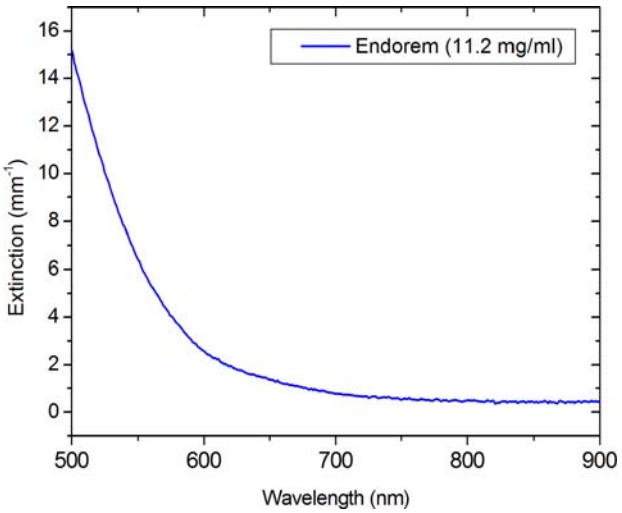

Figure 2 Extinction spectrum of Endorem® (11.2 mg/ml).

replaced by metastatic cells after 10 days and showed initial metastatic involvement after 4 days. Because we aimed to study the changes in SPIO distribution at an earlier stage of metastatic involvement, corresponding with smaller metastases, the inoculation times were set at 5 and 8 days.

Twenty-four hours after SPIO injection the animals were euthanized under anesthesia by cervical dislocation and the popliteal lymph nodes of both hindlegs were dissected. Four popliteal nodes of the contra lateral side were used as controls (control group) because earlier research has proven that these nodes remain free of metastasis within the used inoculation time [35]. In addition to the two tumor groups, two animals received no SPIO injection after 5 days of inoculation (sham group) to verify the PA response in metastatic and normal nodes without SPIOs. After PA and MR imaging, the nodes were embedded in paraffin, cut into 5 μm slices and stained using a normal H & E staining. To visualize the locations of the metastases and compare them with the PA and MR images, one of the nodes was additionally immunohistochemically stained for vimentin. Vimentin, a type III intermediate filament (IF) protein and mesenchymal marker, is specifically suited to stain poorly differentiated and highly metastatic cells like the MAT-lylu line. Attention was paid during sectioning of the tissue to ensure the orientation corresponded with the imaging planes of both PA and MR imaging.

2.2 *Photoacoustic imaging setup*

Resected nodes were placed inside a hollow transparent 3% Agar sample holder with an inner diameter of 25 mm and wall thickness of 10 mm. The sample holder was filled with phosphate buffered saline (PBS) to prevent tissue degradation and placed in the center of a large water container.

The detector was placed orthogonal to the light illumination from the top and rotated around the object to acquire a tomographic measurement. Twenty tomographic projections were acquired for each image using the instrument we described earlier [39]. In summary, the system (Figure 3) consists of a Q-switched Nd : YAG laser (Brilliant B, Quantel, France) with an optical parametric oscillator (Opotek, 700 to 950 nm) operating at a 10 Hz repetition rate. The light is delivered via a beam expander creating a beam diameter of around 1 cm to cover the sample in a top-illumination configuration [40]. An output energy of approximately 20 mJ/cm^2 was used for all scans. The photoacoustic signals are recorded with a curvilinear detector array (Imasonic, Besançon) consisting of 32 elements and shaped to 85° of a circle of 40 mm radius. The center frequency of the array is 6.25 MHz with a reception bandwidth greater than 80%. Individual elements have sizes of 10 by 0.25 mm. These elements are arranged with an inter-element spacing of 1.85 mm. At each position, signals are acquired from the detector using a 32 channel pulse-receiver system (Lecoeur Electronique, Paris, France) with a sampling rate of 80 MHz. Filtered acoustic backprojection was used to reconstruct the PA images.

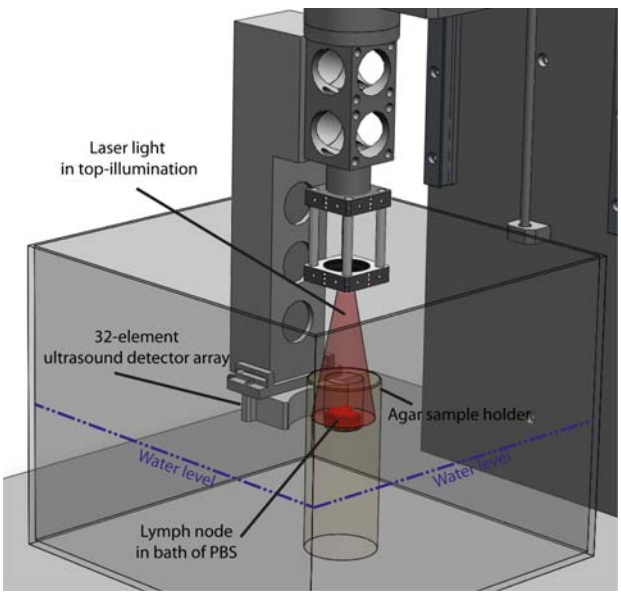

Figure 3 Schematic of the photoacoustic setup. Lymph node samples are placed inside an agar holder and illuminated from the top while the ultrasound detector is rotated around the sample. The entire setup is placed inside a water filled tank to enable wave propagation.

Images were acquired using an excitation wavelength of 720 nm. While 720 nm is not an exclusive wavelength for detecting SPIO's, it combines a low absorption of total hemoglobin with a significant absorption of the SPIO dispersion, while absorption by fat (and water) remains negligible [41]. Furthermore, it allows for a direct comparison with our previous results in healthy animals [34]. Image slice acquisition time of the system for 20 projections is about 60 seconds.

In addition to the single wavelength illumination at 720 nm, multiple wavelength images of two lymph nodes were acquired at 720, 740, 760 and 780 nm. Multiple wavelength information could possibly facilitate the distinction of the SPIO deposits from other biological absorbers in an *in vivo* setting. To this end, the average pixel value of the PA contrast regions within the images was calculated and compared to spectroscopic values of the SPIO dispersion. For comparison, both the spectroscopic data and the average pixel values within the images were normalized.

2.3 Magnetic Resonance imaging

In order to achieve a comparable spatial resolution to our PA images, the nodes were imaged using a 14 Tesla MRI system (Bruker, Ettlingen, Germany) described earlier [34]. Before imaging, the nodes were transferred to quartz NMR tubes with a diameter of 10 mm, and fixated using 4% buffered formaldehyde. All nodes were positioned according to their orientation within the PA setup. A Multi-slice-multi-echo (MSME) imaging sequence was used with an echo time of 10 ms and a repetition time of 1000 ms. The sequence produces a larger longitudinal and transverse magnetization making the surrounding fat appear bright, while SPIO areas appear dark due to rapid reduction of transverse magnetization. This difference facilitates nodal identification and SPIO distribution analysis in the imaged volume. Images were acquired using a matrix dimension of 256×256, a field of view of 1 cm, 25 averages and a slice thickness of 1 mm. MR scan time mounted up to 2 hours per node.

2.4 Contrast quantification

The amount of iron inside the lymphatic tissue was quantified using a vibrating sample magnetometer (VSM) (Quantum Design, San Diego, United States) with a variable magnetic field of ± 4 Tesla. From the measured SPIO amounts a concentration estimation ($\mu g/mm^3$) within each node was calculated by dividing the total iron amount by the volume of the node. Nodal volume was estimated from the dimensions of the nodes in the MR images. The estimated concentration was then correlated to the amount of PA contrast within each nodal image by manually selecting the nodal area within the PA image and calculating the average pixel value of the selection. To exclude large deviations in single pixel values, a 5×5 pixel moving average was first implemented on each PA image. Due to the fact that the detector contains an image slice thickness of approximately 1 mm, the average pixel value (APV) of each selected image region was then divided by its area to produce a "contrast" concentration (APV/mm^3) comparable with the estimated iron concentration.

3. Results

A comparison between the PA and MR images for the different animal groups is shown in Figures 4–6. PA imaging of lymph nodes without contrast agent (both benign and metastatic) (Figure 4) shows that almost no PA response is generated by nodal tissue without the SPIO additive and no clear structures can be distinguished. As a result no clear distinction can be made between nodes with and without metastases. Such a distinction can also not be made based on the corresponding unenhanced MR images. The absence of hypo-intense regions also indicates that no SPIO particles are present within the nodal volume.

The control group (Figure 5) shows that addition of the SPIOs results in a clear and continuous ring of PA contrast in the peripheral zone of the nodes. The ring-like patterns are relatively free of intermissions and show large PA responses throughout their volume compared to the background. The associated MR images contain homogeneous blackening throughout the nodal volume except for the third node (Figure 5(3), red arrow). The blackening within the nodal volume seems to display an uniform distribution and no irregularities are detected. Photos of the paraffin samples show that the discrepancy between MR and PA images could be caused by a sensitivity difference between both modalities as the nodes show a decreased SPIO deposition in their center (Figure 5, purple arrows) which corresponds with the PA images. Shapes and dimensions correspond for both imaging modalities. The detected iron concentrations measured with VSM varies from 2.9 to 4.2 $\mu g/mm^3$ (Table 1). Histology reveals no metastatic cells (Figure 8(1–3)).

The PA images of the nodes in the major metastatic group (Figure 6(1–4)) show an altered contrast distribution. There is an absence of a continuous contrast band together with a lowered PA response. The

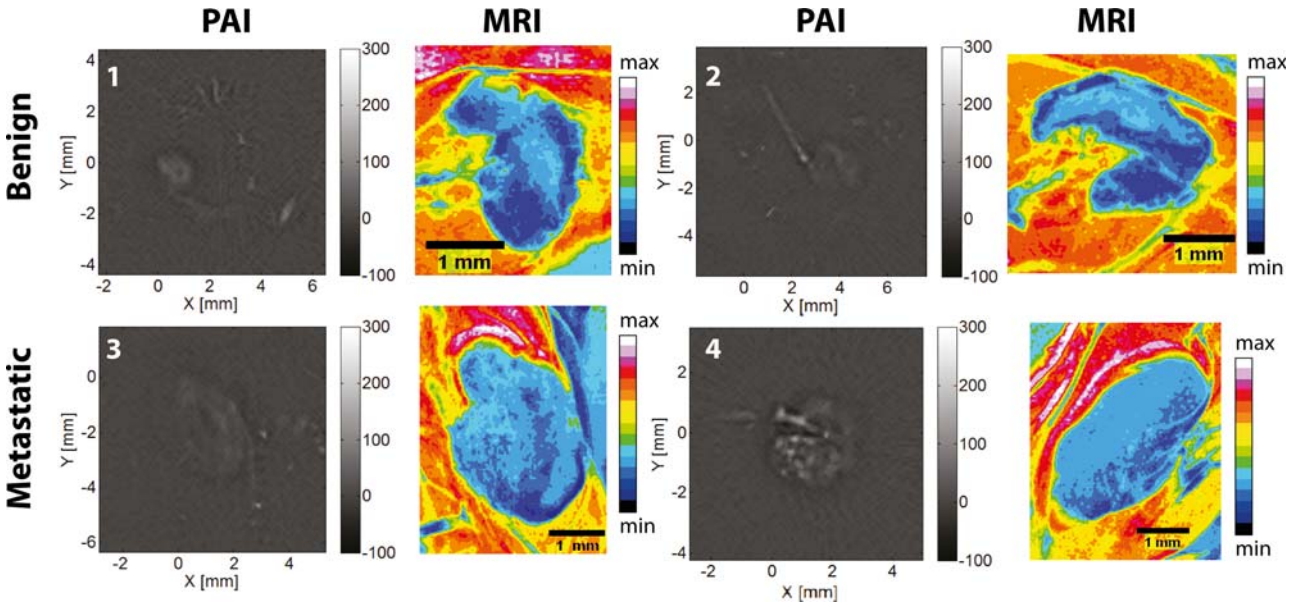

Figure 4 PA and MR image of benign and metastatic nodes without SPIOs (sham group). PAI maps display PA intensity distributions (a.u.) and MR images show signal intensity (a.u.) obtained with a MSME pulse sequence (see materials & methods). The PA contrast between the tissue and the background is small and the nodes are not easily distinguished. The MR images show no hypo-intense regions, corresponding with the absence of SPIOs.

PA signal areas within the images display a discontinuous, irregular distribution with a decreased PA signal response compared to the control nodes (Table 1). MR images show a similar contrast distribution with a lack of hypo-intensity in large areas of the nodal volume (Figure 6, red arrows). In areas displaying the presence of SPIO contrast, the contrast bands seem to be irregular with hyper intensive spots

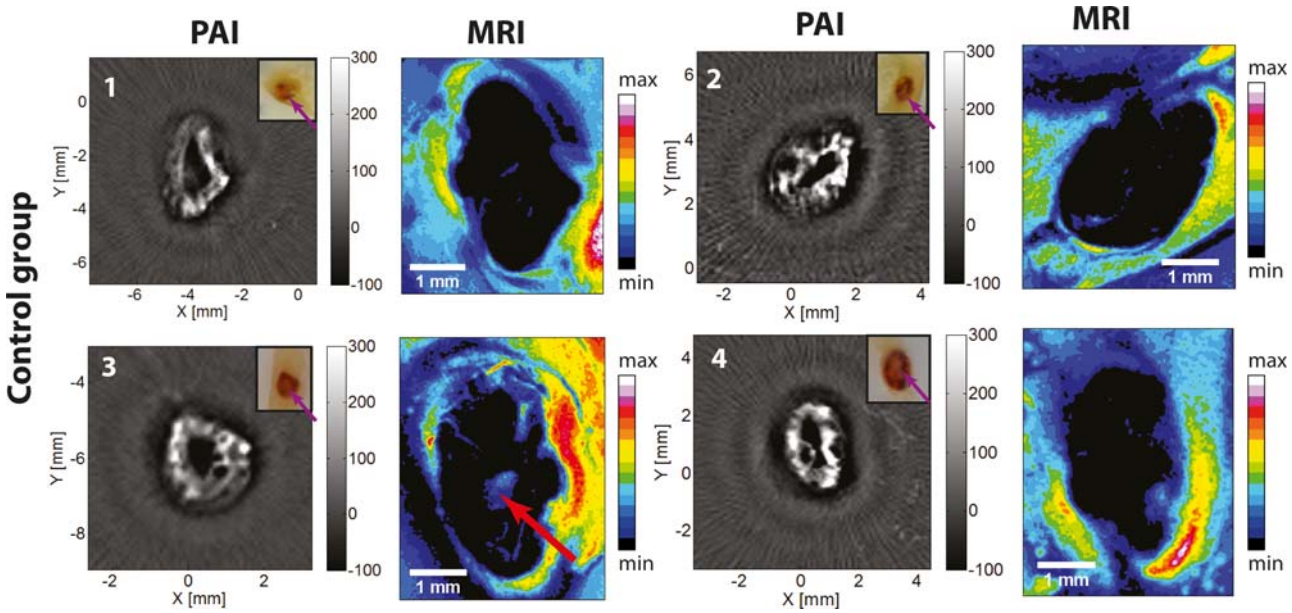

Figure 5 PA and MR images of the control group. The PA images show a clearly distinguishable continuous high contrast band in the peripheral zone of the nodes while MR images display hypointensity throughout the nodal volume, with exception of node 3 (red arrow). Photos of the paraffin sections show that this discrepancy could be caused by sensitivity differences between both modalities, because the central zone of the nodes display a decreased SPIO deposition (purple arrows).

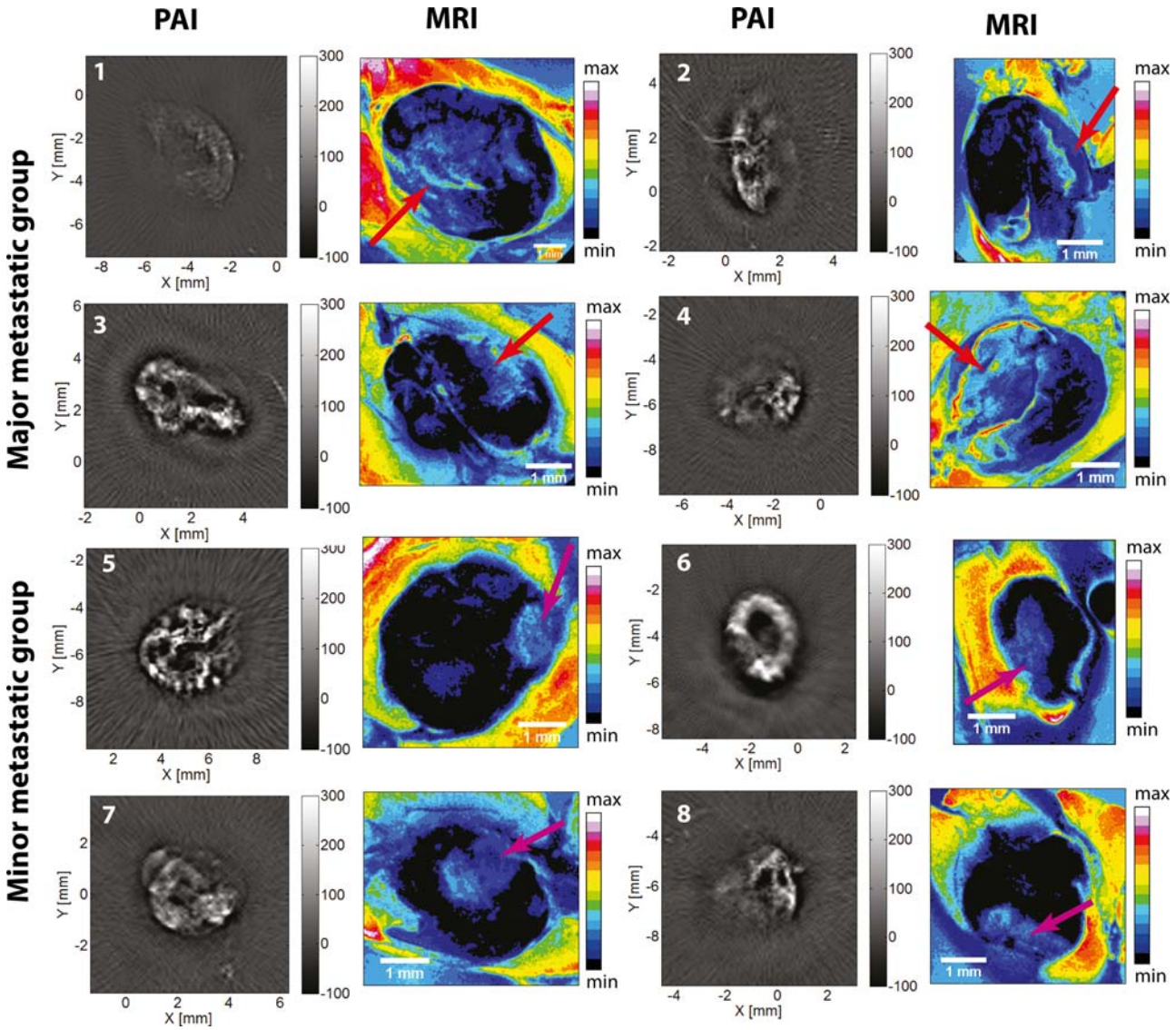

Figure 6 PA and MR images of the metastatic groups. The PA response pattern is grossly comparable to the areas of MR signal decrease in all the nodes. The contrast distribution is irregular compared to the control group with large areas lacking enhancement, especially in the major metastatic group (red arrows). MR and PA contrast patterns grossly compare for all the nodes. In contrast to the other nodes, node 6 seems to contain a regular peripheral contrast band with only a small decreased PA response in the lower left quadrant (purple arrow).

within these contrast areas. Again there is a clear resemblance in contrast distribution between the MR and PA images, as more clearly displayed by a comparison of the images of lymph node 1 (Figure 7). Both maps show a similar lack of contrast in the left lower part of the node while an irregular contrast band is located in the upper right. The iron concentration measured within the nodes of the major metastatic group is also significantly lower compared to the control group with concentrations ranging from 0.4 to 1.0 $\mu g/mm^3$ (Table 1). Histology reveals the presence of metastatic cells (Figure 8(4–6)) in all nodes, although the location of these metastases could not to be matched to all contrast lacking areas in the MR or PA images on a point-to-point basis. This is more clear once the images of lymph node 1 are compared to the vimentin stains (Figure 7). Although the node shows larger metastatic deposits in the lower peripheral zone of the node (red arrows) compared to the upper part (blue arrows), the vimentin map shows that not all contrast lacking areas correspond to metastatic cell deposits.

The PA images of the nodes in the minor metastatic group (Figure 6(5–8)) do also display irregularities in their contrast distribution and a decreased PA response per mm^3 (Table 1). The amount of PA

Table 1 Measured SPIO concentrations and PA contrast within the individual nodes. Nodal numbers correspond to the numbering within the figures.

Control nodes	Iron concentration VSM ($\mu g/mm^3$)	PA contrast in image (mm^{-3})
1	2.9	13.0
2	3.5	9.6
3	4.2	15.6
4	3.6	15.0
Metastatic nodes	**Iron concentration VSM ($\mu g/mm^3$)**	**PA contrast in image (mm^{-3})**
1	0.4	0.8
2	0.6	2.5
3	1.0	5.4
4	0.7	3.8
5	1.6	8.4
6	1.1	6.8
7	1.8	7.5
8	1.7	6.5

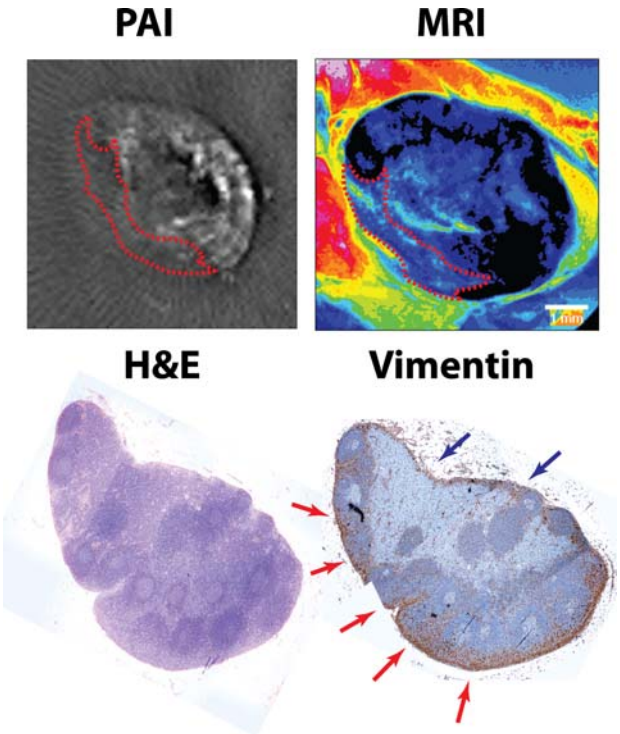

Figure 7 PA and MR images compared with both H & E and Vimentin histology staining for node 1. The contrast distribution between PA and MR is comparable, showing some SPIOs deposits in the upper parts of the node and absence of SPIOs in the lower parts (red dotted line). Localization of the metastatic deposits is difficult to correlate to the images using the H & E staining due to lack of contrast between metastatic cells and lymphocytes. Vimentin staining shows the metastatic deposits more clearly (dark brown) and displays a larger amount of metastatic cells in the lower part of the node (red arrows). Some metastatic cells can be detected in the upper part of the node (blue arrows) but deposits are less pronounced.

contrast per mm^3 has however decreased less than within the major metastatic group (Table 1). The corresponding MR images also show areas which lack the hypo-intensity caused by SPIO presence (Figure 6, purple arrows) and to great extent correlate to the absorption patterns of the PA images. However, the hypo-intense areas seem to be less extensively present than within the major metastatic group. Compared to the other nodes within the group, lymph node 6 displays a more regular contrast distribution with only a minor area of SPIO absence in the left peripheral zone (purple area). Measured iron concentrations of the minor metastatic group lie between the control and major metastatic group ranging from 1.1 to 1.8 $\mu g/mm^3$ (Table 1).

Correlation of the calculated APVs with the measured iron concentrations using the least squares approach for all nodes reveals a strong linear relation between the two (Figure 9), showing a correlation coefficient $R = 0.94$ and a corresponding root mean square of the error (Root MSE) of 1.3. This correlation shows that it could be possible to produce an estimation of the iron concentration by analyzing the PA image contrast within the node.

Multiple wavelength imaging of SPIO containing areas in two of the lymph nodes shows an almost constant average PA response for 720, 740, 760 and 780 nm excitation. This constant response agrees with the extinction spectrum of the SPIO dispersion (Figure 10) which is dissimilar from the varying absorption of hemoglobin in this wavelength range.

4. Discussion

The results demonstrate that there is a difference in both the PA contrast pattern and the PA intensity between resected rat lymph nodes with and without metastatic deposits after subcutaneous SPIO injection. A regular high intensity PA contrast pattern in the periphery of the nodes seems to correspond to an absence of nodal metastases while the presence of metastatic deposits results in a decline of PA signal intensity and the presence of irregularities in the peripheral contrast band. MR imaging shows a similar trend with the presence of larger areas of hyperintensity once the tumor inoculation time is prolonged. These findings correspond with the general theory that SPIO uptake in metastatic lymph nodes is altered due to displacement of peripheral macro-

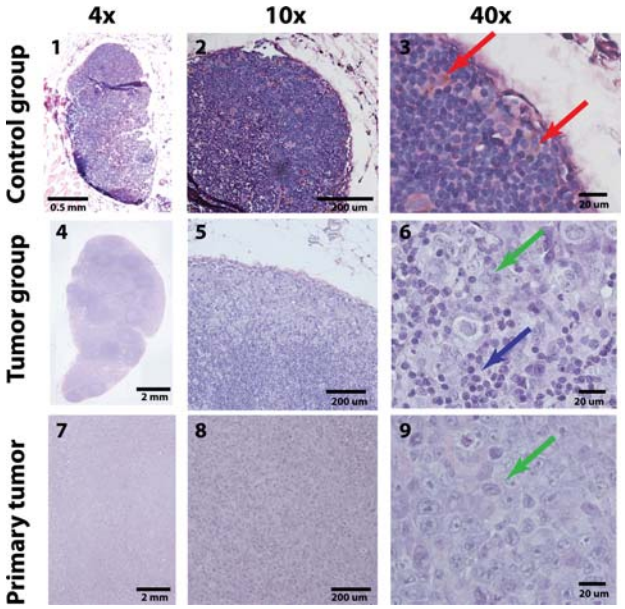

Figure 8 H & E staining of the control and tumor groups together with the primary tumor at 4×, 10× and 40× magnification. The control nodes show the presence of both lymphocytes and macrophages (1–3). SPIO deposits can be seen within the peripheral zone of the node (red arrows). The nodes in the tumor group show metastatic involvement throughout the nodal volume with larger metastatic deposits in the pheripheral zone (4–6). Normal lymphocytes (blue arrow) can still be located near the metastatic cells (green arrow). The metastasic cells correlate well to the poorly differentiated adenocarcinoma cells of the primary tumor (green arrow) (7–9).

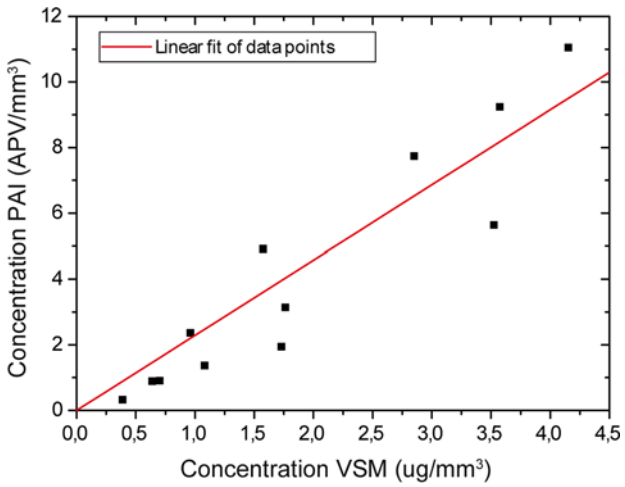

Figure 9 Correlation between the measured iron concentration with VSM and the calculated PA image contrast. Linear fit through 0,0 of the data points (red line) shows a linear correlation between the two parameters ($R = 0.94$, Root MSE = 1.3).

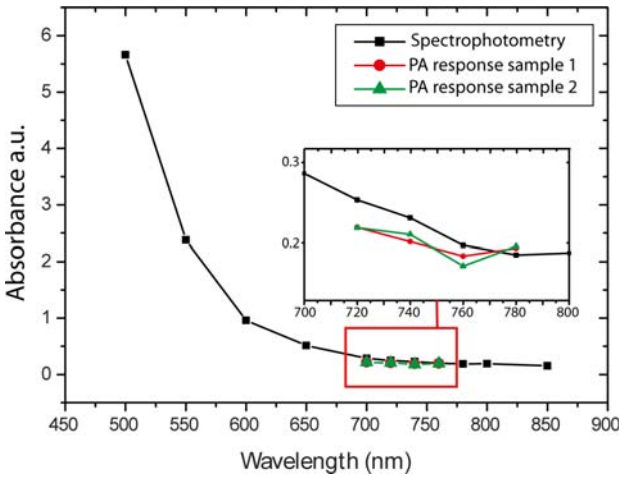

Figure 10 Correlation between the optical extinction of a SPIO dispersion measured with optical spectroscopy (black line) compared to the amount of PA response from two lymph nodes at 4 different excitation wavelengths (green and red line). With the absorbance displayed on a logarithmic scale, the zoomed graph shows that both the optical absorption and PA response are almost constant at the wavelength range from 720 to 780 nm. This constant absorption is not present in other biological chromophores, which might offer additional grounds to distinguish SPIO particles *in vivo*.

phages by metastatic cells as explained by Kimura et al. [42]. To our understanding this is the first time that nodal metastases are visualized with PA imaging using a non-specific clinically approved contrast nanoparticle.

However, one-on-one matching of the PA and MR images with histology does prove challenging as shown in Figure 7. This could be explained by small differences in orientation or the fact that MR and PA images contain slice thicknesses of 1 mm while histological slides are only 5 μm. Its leads us to conclude that PA images should not be viewed as an exact metastatic map, but that alterations in the absorption pattern should be interpreted as indications of metastatic involvement within the nodal volume. Although this might decrease the eventual sensitivity of the technique for smaller metastases, recent data from the American College of Surgeons Oncology Group Z0011 trial gives some indication that small metastatic deposits in lymph nodes are of limited importance for the clinical outcome of, for example, breast cancer patients [43]. Although there remains some discussion about the implications of the trial, the fact that the detection of these deposits might be of minor importance compared to macro-metastases, could make the application of the method for rapid intra-operative screening especially applicable for breast cancer patients. The technique then offers the additional advantage that post-operative analysis re-

mains possible because the tissue is left intact by the imaging procedure and can still be processed for histology. This would then permit additional lymph node removal once histology reveals that metastases have been missed.

In contrast to the indication that a regular PA contrast distribution combined with a high signal intensity seems to correspond to a healthy node, one of the metastatic nodes, namely number 6, also shows a relatively regular and intensive PA band. The absence of contrast in the lower left part of the node (purple arrow) represents the only irregular observation in both PA and MR images, making it challenging to define to which extent metastases have to be progressed before they can be sensitively detected with this approach. On the other hand, small areas of PA signal absence in benign nodes might also lead to a wrong metastatic diagnosis which could give the technique a higher false positive rate. These unknowns warrant the claim for additional research with larger sample numbers on lymph nodes harboring early metastatic involvement which could provide more information whether in most cases the metastatic induced phagocytotic changes will result in detectable alterations of the PA contrast map and how this has impact on the sensitivity and specificity of the technique.

The MR and PA images show clear similarities in the distribution of SPIO contrast, indicating that SPIO distributions can also be accurately mapped using photoacoustics. With regard to image quality, the MRI system is superior compared to the tomographic PA system, but it has to be taken into account that MR image acquisition requires several hours. Furthermore, a comparable MR setup is not only expensive and bulky but also contains a strong magnetic field which is unsuitable for an intra-operative setting. These advantages emphasize the possible additional benefit of a PA approach.

The decrease in PA intensity within the metastatic nodes corresponds to a measured decrease in iron concentration (Table 1). The iron concentrations measured with VSM show a decline in SPIO uptake depending on the length of the primary tumor inoculation time. PA contrast amounts are shown to have a strong linear relationship ($R = 0.94$) with the iron concentrations indicating that the PA intensity could be converted into an estimation for the iron amount. Although this remains to be a qualitative estimation because the actual photon fluence within the tissue is unknown, more quantitative approaches could possibly be implemented including an ultrasound modulated fluence correction approach [44]. For now, the fact that PA intensity per mm^3 seems to be decreased in metastatic nodes, which can be linked to a decreased iron concentration, shows that PA intensity measurements could possibly be used as an additional tool for nodal assessment.

The fact that the control lymph nodes are smaller and contain less immune cells than the nodes within the tumor groups could raise some questions about the applicability of the technique for large reactive nodes. These nodes could for example be present once the immune system reacts to the presence of a primary tumor. Although we stress the importance of further research, results in a healthy animal model in which reactive nodes were induced by incomplete Freund Adjuvant injection also showed the presence of regular high intensity peripheral PA contrast bands [34]. This seems to indicate that the uptake of SPIOs by the peripheral macrophages is unaltered even if tumor induced reactivity results in the presence of more immune cells and swelling of the node. The technique might therefore also be suitable for larger or activated lymph nodes.

Finally, even though the results demonstrate the potential of an intra-operative PA application for resected *ex vivo* nodal staging, the use of SPIOs in an *in vivo* setting could also be considered. In such a setting, the fact that smaller SPIO deposits generate lower PA response [45] could be compensated by differentiation on the basis of multiple wavelength excitation. The constant PA response of the SPIOs in the near-infrared (Figure 10) is dissimilar from the varying absorption of oxy- and deoxyhemoglobin, providing some grounds to separate the PA signals of both. Future research will be directed towards such a spectral method, which should verify if SPIOs could also contain *in vivo* applicability.

5. Conclusion

The use of a tomographic PA setup together with a subcutaneously injected, clinically approved SPIO dispersion is capable of distinguishing benign from metastatic nodes in an *ex vivo* setting. Indications for metastatic involvement seem to be a lowered and irregular PA intensity pattern which can be linked to a decreased SPIO concentration and distribution. These results pave the way for a clinical exploratory study into the accuracy of the technique for intra-operative staging.

Acknowledgements We acknowledge the contribution of dr. J. Jose for his insights in the photoacoustic imaging procedure and thank Ms. B. Klomphaar for her help regarding animal care. Additionally we thank the experimental urology department of the Radboud University Nijmegen for generously supplying us with the MAT-lylu cell line. The work was funded by the MIRA institute for Biomedical Technology and Technical Medicine.

Author biographies Please see Supporting Information online.

References

[1] A. Govindarajan and N. N. Baxter, Clin Colorectal Cancer **7**(4), 240–246 (2008).
[2] A. E. Giuliano, D. M. Kirgan, J. M. Guenther, and D. L. Morton, Ann Surg **220**(3), 391–398; discussion 398–401 (1994).
[3] D. L. Morton, D. R. Wen, J. H. Wong, J. S. Economou, L. A. Cagle, F. K. Storm, L. J. Foshag, and A. J. Cochran, Arch Surg **127**(4), 392–399 (1992).
[4] M. J. Liptay, Ann Surg Oncol **11**(Suppl. 3), 271S–274S (2004).
[5] C. M. Balch, S. J. Soong, J. E. Gershenwald, J. F. Thompson, D. S. Reintgen, N. Cascinelli, M. Urist, K. M. McMasters, M. I. Ross, J. M. Kirkwood, M. B. Atkins, J. A. Thompson, D. G. Coit, D. Byrd, R. Desmond, Y. Zhang, P. Y. Liu, G. H. Lyman, and A. Morabito, J Clin Oncol **19**(16), 3622–3634 (2001).
[6] D. N. Krag and R. M. Single, Ann Surg Oncol **10**(10), 1152–1159 (2003).
[7] M. G. Harisinghani, J. Barentsz, P. F. Hahn, W. M. Deserno, S. Tabatabaei, C. H. van de Kaa, J. de la Rosette, and R. Weissleder, N Engl J Med **348**(25), 2491–2499 (2003).
[8] O. Will, S. Purkayastha, C. Chan, T. Athanasiou, A. W. Darzi, W. Gedroyc, and P. P. Tekkis, Lancet Oncol **7**(1), 52–60 (2006).
[9] O. Clement, N. Siauve, C. A. Cuenod, and G. Frija, Top Magn Reson Imaging **9**(3), 167–182 (1998).
[10] M. Taupitz, S. Wagner, and B. Hamm, Radiologe **36**(2), 134–140 (1996).
[11] L. V. Wang and S. Hu, Science **335**(6075), 1458–1462 (2012).
[12] D. Razansky, N. C. Deliolanis, C. Vinegoni, and V. Ntziachristos, Curr Pharm Biotechnol **13**(4), 504–522 (2012).
[13] M. Heijblom, D. Piras, W. Xia, J. C. van Hespen, J. M. Klaase, F. M. van den Engh, T. G. van Leeuwen, W. Steenbergen, and S. Manohar, Opt Express **20**(11), 11582–11597 (2012).
[14] S. A. Ermilov, T. Khamapirad, A. Conjusteau, M. H. Leonard, R. Lacewell, K. Mehta, T. Miller, and A. A. Oraevsky, J Biomed Opt **14**(2), 024007 (2009).
[15] R. A. Kruger, R. B. Lam, D. R. Reinecke, S. P. Del Rio, and R. P. Doyle, Med Phys **37**(11), 6096–6100 (2010).
[16] M. Jaeger, S. Preisser, M. Kitz, D. Ferrara, S. Senegas, D. Schweizer, and M. Frenz, Phys Med Biol **56**(18), 5889–5901 (2011).
[17] C. M. O'Brien, K. Rood, S. Sengupta, S. K. Gupta, T. DeSouza, A. Cook, and J. A. Viator, J Vis Exp **57**, e3559 (2011).
[18] J. Jose, D. J. Grootendorst, T. W. Vijn, M. Wouters, H. van Boven, T. G. van Leeuwen, W. Steenbergen, T. J. Ruers, and S. Manohar, J Biomed Opt **16**(9), 096021 (2011).
[19] D. J. Grootendorst, J. Jose, M. W. Wouters, H. van Boven, J. Van der Hage, T. G. Van Leeuwen, W. Steenbergen, S. Manohar, and T. J. Ruers, Lasers Surg Med **44**(7), 541–549 (2012).
[20] G. P. Luke, D. Yeager, and S. Y. Emelianov, Ann Biomed Eng **40**(2), 422–437 (2012).
[21] S. Manohar, C. Ungureanu, and T. G. Van Leeuwen, Contrast Media & Mol Imaging **6**(5), 389–400 (2011).
[22] G. M. Lanza, Contrast Media Mol Imaging **6**(5), 331 (2011).
[23] N. Kosaka, M. Bernardo, M. Mitsunaga, P. L. Choyke, and H. Kobayashi, Contrast Media Mol Imaging **7**(2), 247–253 (2012).
[24] B. Ballou, L. A. Ernst, S. Andreko, T. Harper, J. A. Fitzpatrick, A. S. Waggoner, and M. P. Bruchez, Bioconjug Chem **18**(2), 389–396 (2007).
[25] K. Yang, L. Hu, X. Ma, S. Ye, L. Cheng, X. Shi, C. Li, Y. Li, and Z. Liu, Adv Mater **24**(14), 1868–1872 (2012).
[26] K. H. Song, C. Kim, K. Maslov, and L. V. Wang, Eur J Radiol **70**(2), 227–231 (2009).
[27] K. H. Song, E. W. Stein, J. A. Margenthaler, and L. V. Wang, J Biomed Opt **13**(5), 054033 (2008).
[28] T. N. Erpelding, C. Kim, M. Pramanik, L. Jankovic, K. Maslov, Z. Guo, J. A. Margenthaler, M. D. Pashley, and L. V. Wang, Radiology **256**(1), 102–110 (2010).
[29] E. I. Galanzha, E. V. Shashkov, P. M. Spring, J. Y. Suen, and V. P. Zharov, Cancer Res **69**(20), 7926–7934 (2009).
[30] W. J. Akers, W. B. Edwards, C. Kim, B. Xu, T. N. Erpelding, L. V. Wang, and S. Achilefu, Transl Res **159**(3), 175–181 (2012).
[31] D. Pan, X. Cai, C. Yalaz, A. Senpan, K. Omanakuttan, S. A. Wickline, L. V. Wang, and G. M. Lanza, ACS Nano **6**(2), 1260–1267 (2012).
[32] R. A. McLaughlin, L. Scolaro, P. Robbins, S. Hamza, C. Saunders, and D. D. Sampson, Cancer Res **70**(7), 2579–2584 (2010).
[33] J. D. Horsnell, J. A. Smith, M. Sattlecker, A. Sammon, J. Christie-Brown, C. Kendall, and N. Stone, Surgeon **10**(3), 123–127 (2012).
[34] D. J. Grootendorst, J. Jose, R. M. Fratila, M. Visscher, A. H. Velders, B. Ten Haken, T. G. Van Leeuwen, W. Steenbergen, S. Manohar, and T. J. Ruers, Contrast Media Mol Imaging **8**(1), 83–91 (2013).
[35] P. Vassallo, C. Matei, W. D. Heston, S. J. McLachlan, J. A. Koutcher, and R. A. Castellino, Invest Radiol **30**(12), 706–711 (1995).
[36] W. M. Klerkx, A. A. Geldof, A. P. Heintz, P. J. van Diest, F. Visser, W. P. Mali, and W. B. Veldhuis, J Magn Reson Imaging **33**(5), 1151–1159 (2011).
[37] F. Cengelli, D. Maysinger, F. Tschudi-Monnet, X. Montet, C. Corot, A. Petri-Fink, H. Hofmann, and L. Juillerat-Jeanneret, J Pharmacol Exp Ther **318**(1), 108–116 (2006).
[38] Y. X. Wang, S. M. Hussain, and G. P. Krestin, Eur Radiol **11**(11), 2319–2331 (2001).
[39] J. Jose, R. G. Willemink, S. Resink, D. Piras, J. C. van Hespen, C. H. Slump, W. Steenbergen, T. G. van Leeuwen, and S. Manohar, Opt Express **19**(3), 2093–2104 (2011).
[40] Y. Lao, D. Xing, S. Yang, and L. Xiang, Phys Med Biol **53**(15), 4203–4212 (2008).
[41] P. Beard, Interface Focus **1**(4), 602–631 (2011).

[42] K. Kimura, N. Tanigawa, M. Matsuki, T. Nohara, M. Iwamoto, K. Sumiyoshi, S. Tanaka, Y. Takahashi, and Y. Narumi, Breast Cancer **17**(4), 241–246 (2010).
[43] V. Galimberti, C. Chifu, S. Rodriguez Perez, P. Veronesi, M. Intra, E. Botteri, M. Mastropasqua, M. Colleoni, A. Luini, and U. Veronesi, Breast **20**(Suppl. 3) S96–S98 (2011).
[44] K. Daoudi, A. Hussain, E. Hondebrink, and W. Steenbergen, Opt Express **20**(13), 14117–14129 (2012).
[45] M. P. Mienkina, C. S. Friedrich, K. Hensel, N. C. Gerhardt, M. R. Hofmann, and G. Schmitz, Biomed Tech (Berl) **54**(2), 83–88 (2009).

